Schwaighofer, E.; Staron, P.; Rashkova, B.; Stark, A.; Schell, N.; Clemens, H.; Mayer, S.:

In situ small-angle X-ray scattering study of the perovskite-type carbide precipitation behavior in a carbon-containing intermetallic TiAl alloy using synchrotron radiation

In: Acta Materialia (2014) Elsevier

DOI: 10.1016/j.actamat.2014.06.017

In situ small-angle X-ray scattering study of the perovskite-type carbide precipitation behavior in a carbon-containing intermetallic TiAl alloy using synchrotron radiation

Emanuel Schwaighofer [a,⇑], Peter Staron [b], Boryana Rashkova [a], Andreas Stark [b], Norbert Schell [b], Helmut Clemens [a], Svea Mayer [a]

[a] Department of Physical Metallurgy and Materials Testing, Montanuniversita¨ t Leoben, Roseggerstraße 12, A-8700 Leoben, Austria

[b] Institute of Materials Research, Helmholtz-Zentrum Geesthacht, Max-Planck-Straße 1, D-21502 Geesthacht, Germany

Received 14 February 2014; received in revised form 5 June 2014; accepted 6 June 2014
Available online 5 July 2014

Abstract

Intermetallic c-TiAl based alloys of the latest generation, e.g. TNM alloys with a nominal composition of Ti–43.5Al–4Nb–1Mo–0.1B (in at.%), exhibit the potential to be used in modern high-performance combustion engines due to their low density, high strength and creep resistance as well as their good oxidation properties at elevated temperatures. Alloying with C can further improve the hightemperature performance by both solid solution hardening and/or carbide formation. In this study, starting from a supersaturated TNM–1C alloy the precipitation behavior and thermal stability of perovskite-type carbides Ti_3AlC during isothermal annealing and ensuing re-heating to 1200 _C are quantified by means of an in situ small-angle X-ray scattering experiment using synchrotron radiation. Complementarily, the formed hierarchical structures on the nano-scale, i.e. p-type carbide precipitates within ultra-fine c-lamellae of the a_2/c-colonies, were investigated by means of monochromatic high-energy X-ray diffraction in combination with scanning and transmission electron microscopy. Additionally, an explanation of an obtained diffraction phenomenon is given, i.e. streak formation that is caused by the very small lamellar spacing of the c-phase within the a_2/c-colonies. It was also found that the geometrically well-define nanostructure allows a correlation between the c-lath thickness and a characteristic dimension of p-type carbides.

Keywords: Intermetallics; Titanium aluminides; Carbon; Precipitation hardening; X-ray synchrotron radiation

1. Introduction

In the last two decades c-TiAl based alloys have been implemented for application as turbine blades and turbocharger wheels in modern high-performance combustion engines due to their attractive properties, e.g. low density of _4 g cm_{-3} combined with enhanced high-temperature (HT) strength and creep resistivity up to 750 _C as well as their good oxidation behavior [1–3]. A further step to improve the HT capability of advanced intermetallic c-TiAl based alloys, such as TNM alloys with a nominal composition of Ti–43.5Al–4Nb–1Mo–0.1B, is alloying with carbon [4–7]. Note that all compositions are stated in at.%. Thereby, C can act as an efficient solid solution strengthener [8] or form needle-shaped precipitates of perovskite-type Ti_3AlC carbides which are finely dispersed in the c-phase [6,7,9]. As a powerful tool for studying phase transformations and the precipitation behavior of minor phases from a supersaturated matrix, e.g. p-type carbides, high-energy

E-mail address: emanuel.schwaighofer@unileoben.ac.at (E. Schwaighofer).

X-ray diffraction (HEXRD) can be applied. Furthermore, in situ performed small-angle X-ray scattering (SAXS) can give a deeper insight into the precipitation kinetics and thermal stability when p-type carbides are arranged continuously in the c-matrix. Additionally, complementary information can be gained from transmission electron microscopy (TEM), i.e. size, orientation and morphology of p-type carbides, which is needed for the evaluation and validation of SAXS measurements. Moreover, the size of c-lamellae within the a_2/c-colonies is suggested to contribute to the appearance of the HEXRD pattern, i.e. streaking, but the mechanism behind this has not been clarified yet [10]. Aging at low temperatures, e.g. at 750 _C, of a supersaturated TiAl material leads to the formation of an ultra-fine hierarchical structure, i.e. fine c-lamellae with a typical thickness of 10–100 nm wherein p-type carbides are finely precipitated [7]. The formed nanostructure depends on the specific orientation relationships between the constituting phases. Thus, the extremely small characteristic dimensions of these microstructural constituents can lead to a broadening of the HEXRD reflections. Therein, the peak broadening can be quantified by means of the so-called Scherrer equation [11,12]:

$$L = K \lambda / \beta \cos \Theta \qquad (1)$$

where L is the crystallite size; K represents the shape factor, taking values between 0.62 and 2.08 [12,13]; λ is the wavelength; β the full width at half maximum (FWHM); and Θ denotes the Bragg angle of the center of the considered diffraction peak.
The SAXS measurements are evaluated by means of the two-phase model according to the small-angle neutron scattering (SANS) experiments as reported in Ref. [9]. Thus, the macroscopic differential scattering cross-section dΣ/dΩ is given as, e.g. [14]:

$$\frac{d\Sigma}{d\Omega}(q) = (\Delta\eta)^2 \int_0^\infty n(R) \cdot V(R)^2 \cdot F(q,R)^2 \cdot dR \tag{2}$$

Here, Δη is the difference of the scattering length densities (SLDDs) of the matrix and the precipitates, n(R) relates to the number density of precipitated particles with a size between R and R + dR, V(R) is the precipitation volume and F(q,R) corresponds to the form factor, wherein the absolute value of the scattering vector is defined as $q = 4\pi/\lambda \sin\Theta$.

2. Material and experimental

The material for the current study was produced by GfE Metalle und Materialien GmbH, Germany, as described in Ref. [7] and has a chemical composition of Ti–43.35Al–4.06Nb–1.02Mo–0.11B–1.02C. Subsequent to ingot metallurgy, the TNM–1C material was hot-isostatically pressed (HIP) at 1200 °C for 4 h followed by furnace cooling (FC). The material exhibits a polycrystalline and fine-grained microstructure due to the precipitation of coarse-grained h-type carbides Ti_2AlC during the solid state phase transformations subsequent to peritectic solidification as reported in Ref. [7]. Especially the fine-grained microstructure is a necessary precondition for reliable examination by means of monochromatic X-ray radiation.

The precipitation kinetics, size evolution and thermal stability of p-type carbides were studied by means of an in situ SAXS experiment conducted at the HZG-operated beamline HEMS, using the experimental hutches P07-EH 3 and EH 4, at the Petra III storage ring of the synchrotron facility DESY in Hamburg, Germany. A sketch of the experimental setup is shown in Fig. 1. A cylindrical sample with a diameter of 5 mm and a length of 10 mm length was inductively heated in an adapted quenching and deformation dilatometer DIL 805 A/D of Bähr Thermoanalyse, Germany, according to the temperature–time (T–t) evolution given in Fig. 2. The monochromatic X-ray beam had a size of 0.8 x 0.8 mm^2 and a wavelength of 0.12398 Å. The scattering data were recorded by employing a mar345 image plate detector from Marresearch, Germany, with a sample-to-detector distance of 11.654 m and an exposure time of 40 s. Due to the detector characteristics, the in situ SAXS measurements could be performed with a frame rate of 20 images h^{-1}. Slits made of pure tungsten minimized undesired scattering from the slits and thus ensured a low background. Data evaluation was performed by means of the program Fit2D with respect to azimuthal integration [15,16] followed by a fitting procedure of the derived scattering curves with the program SANSFit based on a least-square method iteration as conducted in Ref. [9]. The sample-to-detector distance of the SAXS measurements was calibrated by means of an Ag-Behenate standard, while the macroscopic scattering cross-section was calibrated by means of the known precipitated volume fraction of p-type carbides after annealing at 750 °C for 4 h, which was determined by Rietveld analysis of the diffraction data. Due to the maximum content of p-type carbides of <5 vol.%, effects arising from interparticle interference are expected to be negligible. The p-type precipitates were modeled as prolate ellipsoids of revolution with axes of 2R, 2μR, where R is the radius of the elongated particle with a size aspect ratio l = 7 [9]. The particles are suggested to be randomly oriented within the polycrystalline sample obeying a lognormal size distribution [9]. According to the two-phase model in Eq. (2) the scattering contrast primary depends on the difference of the chemical compositions of the γ-phase matrix and the precipitated p-type carbide particles. The SLDD, which corresponds to the scattering contrast, can be calculated according to $\eta_m - \eta_p$, where η_m and η_p are the scattering length densities (SLDs) of matrix and particles, respectively. Generally, η is given as the phase specific quotient of the coherent scattering length b_c and the mean volume per atom ν_a. For TNM alloys the SLDD between the c-phase and the p-type carbide Ti_3AlC was determined to be (1.27 ± 0.03) x 10^{11} cm^{-2} using phase compositions of Ti–46Al–3Nb–1Mo–0.25C with a density of q = 4.40 g cm_{-3} and Ti–20Al–3Nb–1Mo–20C with q = 4.57 g cm^{-3}, respectively. The error in SLDD arises mainly from uncertainties in the composition. Thereby, the composition of the c-phase was derived from JEOL 2100F TEM energy dispersive X-ray spectroscopy

(EDS) microanalysis performed with an INCA system from Oxford Systems, UK, whereas the accompanying Rietveld analysis gives information about the phase densities. The composition of p-type carbides was estimated from its stoichiometry Ti_3AlC with additions of Nb and Mo.

Complementary, ex situ investigations were conducted on specimens 5 mm in diameter and 10 mm in length, which were heat-treated in a chamber furnace RHF 1600 from Carbolite, Great Britain, with calibrated type S thermocouples for temperature control. The various samples were prepared according to the time–temperature profile as given in Fig. 2 and the following materials conditions were adjusted: (a) supersaturated condition, (b) isothermally annealed state (750 _C for 4 h) and (c) re-heated to 1200 _C and subsequently quenched to room temperature (RT).

HEXRD measurements were performed on heat-treated sample material at the HEMS beamline, P07-EH3, for phase identification and quantitative phase analysis using a mean photon energy of 100 keV and a beam size of 0.8 _ 0.8 mm^2. The diffraction data were recorded on an XRD 1622 flat panel detector from Perkin Elmer, USA. There, the experimental setup, i.e. sample-to-detector distance, detector tilt angle and instrumental broadening of reflections, was calibrated using a texture-free LaB_6 standard with no contribution to peak broadening. For the determination of the crystallite size from the streaking of the phase-specific reflections according to Eq. (1) a shape factor of K = 0.89 was used. To this end, the FWHM was corrected with respect to broadening of the instrument.

Furthermore, real-space imaging by means of scanning electron microscopy (SEM) in back-scattered electron (BSE) mode with a EVO 50 from Zeiss, Germany, and TEM investigations in bright-field and diffraction mode with a CM 12 from Philips, Netherlands, operated at an acceleration voltage of 120 kV were applied for the evaluation of the prevailing microstructures and the verification of the characteristic dimensions of c-lamellae and p-type carbides, as expected from HEXRD and in situ SAXS experiments. Additional Vickers macrohardness measurements were performed with a M4C 025 G3 M from Emco-Test, Austria, with an accuracy of ±5 HV10, quantifying the influence of microstructural features on mechanical properties, i.e. correlation of RT hardness with yield strength according to Ref. [17].

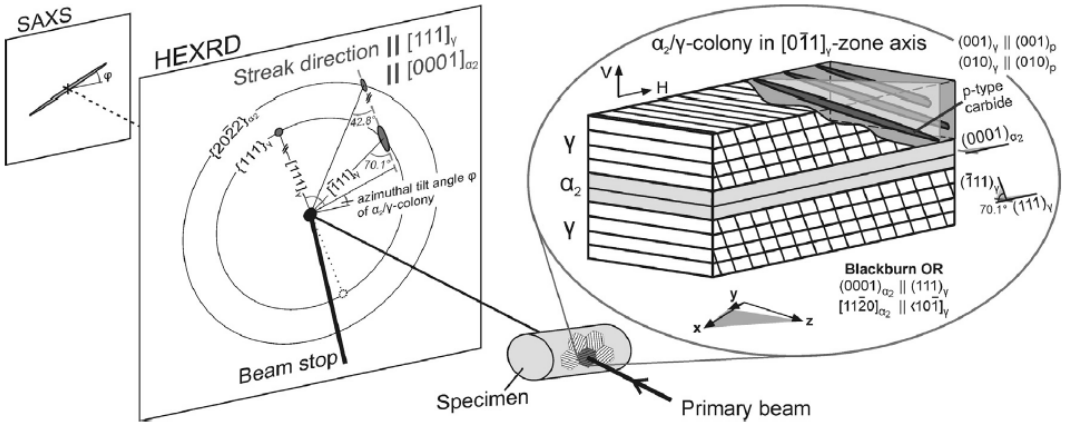

Fig. 1. Experimental setup of the conducted synchrotron experiment at the HZG-operated beamline HEMS, P07, at Petra III. The monochromatic beam with a mean energy of 100 keV is guided through the sample, which is situated in a modified quenching and deformation dilatometer device. The diffraction patterns are recorded with a Perkin Elmer XRD 1622 flat panel detector in experimental hutch EH 3 (HEXRD), whereas a mar345 Image Plate detector located behind in EH 4 is used to record the signal from small-angle scattering (SAXS). H = horizontal, V = vertical (related to crystal-coordinate system of the c-phase). For explanations see text.

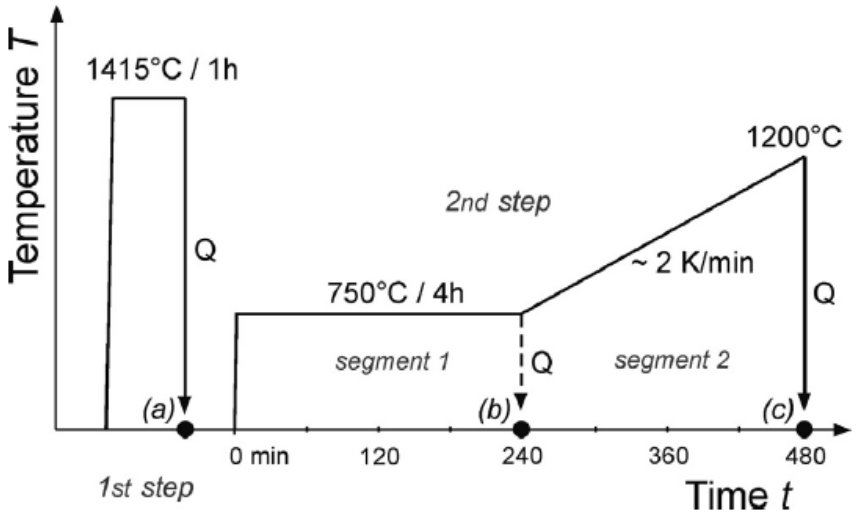

Fig. 2. Temperature–time history of the sample material. The first heat treatment step was conducted ex situ employing a HT furnace due to enhanced risk of thermocouple tear-off and to improve the time-efficiency at the beamline, whereas the second precipitation annealing step was investigated by means of an in situ SAXS experiment using synchrotron radiation. The characteristic heat-treatment conditions at RT (d) are indicated with (a), (b) and (c). Q stands for the quench step.

3. Results and discussion

3.1. Heat-treatment history and microstructural evolution

The heat treatments were performed starting from the cast/HIP microstructure as reported in Ref. [7]. During solidification and subsequent HIPing, coarse-grained h-type carbides Ti_2AlC (space group $P6_3/mmc$) are precipitated, leading to the formation of a fine-grained and texture-free microstructure of the peritectic solidifying TNM–1C alloy which, at RT, primarily consists of γ-TiAl ($L1_0$-structure) and ordered α_2-Ti_3Al ($D0_{19}$-structure) phases as well as minor amounts of ordered β_o-TiAl phase (B2-structure). It was shown that the α_2-phase exhibits a C-solubility about six times higher when compared to the γ-phase, whereas the β_o-phase still has no solubility for C [7,8].

The T–t evolution of the two-step heat treatment is shown in Fig. 2. In the first annealing step the sample material was heat-treated for 1 h at 1415 °C in the (α + β)-phase field region above the solvus temperature of the h-type carbide T_{hsolv}, which was determined to be 1410 °C [7]. Therefore, during isothermal annealing only the disordered phases α-Ti(Al) (A3-structure) and β-Ti(Al) (A2-structure) are thermodynamically stable, where the β-phase suppresses excessive grain growth of the α-phase. Subsequent quenching with a rate >200 K $s_{\_1}$ leads to the formation of a microstructure predominantly consisting of supersaturated α_2-grains ($\alpha_{2,ss}$) with a volume fraction of >95% as depicted in the SEM micrograph shown in Fig. 3a. Here, alloying with C causes decelerated precipitation kinetics of the γ-phase yielding to completely supersaturated and ordered α_2-grains, as shown in the corresponding two dimensional (2-D) diffraction pattern in Fig. 4a. Due to the low amount of grain-growth-inhibiting β-phase of _4 vol.%, coarsened α_2-grains generate large diffraction spots within the polycrystalline and untextured TNM–1C sample material (Fig. 4a). From Figs. 3a and 4a it is also evident that a residual but minor fraction of h-type carbides remains within the supersaturated microstructure after quenching due to annealing close to T_{hsolv}. Thus, residual h-type carbides and Ti-borides (B27-structure) with a cumulative content of _1 vol.% have an additional contribution to the suppression of a-grain growth during annealing. Taking a deeper insight into the b_o-phase of the quenched microstructure reveals the occurrence of an α_{02}-phase ($D0_{19}$-structure) [18] showing a martensitic-type arrangement (α_{2M}) as indicated in the insert of the SEM micrograph in Fig. 3a. Obviously, fast quenching leads to an athermal re-transformation from β- to α-phase, falsifying the phase fractions present during annealing when the subsequent evaluation takes place at RT. Before precipitation annealing, the supersaturated microstructure in Fig. 3a exhibits a macrohardness of 404 HV10 corresponding to a yield strength of 820 MPa, which is in good accordance with the microstructures of a C-free TNM alloy as reported in Ref. [7].

Subsequently, the supersaturated TNM–1C sample material was conducted to an isothermal stabilization or precipitation annealing step at 750 _C for 4 h (see the T–t process in Fig. 2). The corresponding microstructure after quenching to RT is depicted in Fig. 3b. During annealing the supersaturated a2-grains transform to a lamellar α2/γ-phase compound (α2/γ)lam, i.e. α2/γ-colonies with a volume fraction of >95% have formed. Here, the γ-phase precipitates are in the form of very fine lamellae according to the Blackburn relationship (0001)α2 || {1 11}γ and h11_20iα2 || h101]γ [19]. Within the βo-phase, lens-shaped γ-particles are formed according to a modified Kurdjumov–Sachs relationship {1 10}β || {111}γ and h111iβ || - h101]γ [20]. In total, a c-phase content of 74 vol.% is precipitated during isothermal annealing. The diffraction pattern in Fig. 4b indicates the occurrence of p-type carbides Ti3AlC (space group Pm-3m) precipitated within the γ-phase due to its significant lower solubility for C [6–8] in accordance with the orientation relationship (OR) (00 1)γ || (001)p and (010)γ || (010)p as reported in Ref. [5]. Thereby, p-type carbides take a total volume content of 1.9%, which corresponds to a volume fraction of 2.5% in relation to the c-phase. Both the precipitation of

γ-lamellae within the α2-grains as well as p-type carbides within the c-laths lead to an increase of macrohardness of ≈37 HV10, correlating with a relative gain in hardness of 9%, and a total hardness 441 HV10 is obtained. Thus, precipitation annealing leads to an increase of yield strength up to 930 MPa when compared to Ref. [17]. There, the C-free TNM alloy in a comparable heat treatment condition exhibits a macrohardness of 427 HV10, leading to the conclusion that the contribution of p-type carbides to a gain in yield strength is rather small. Contrarily, the precipitation of p-type carbides was found to be efficient, reducing the mobility of dislocations during creep experiments within the power-law regime [6,7]. Furthermore, after isothermal annealing at 750 °C no indication of the formation of xo-phase (B82-structure) was found, as shown for a C-free TNM alloy during heat treatments and creep testing experiments below 825 °C, which corresponds to the solvus temperature of the ωo-phase [21]. In conclusion, alloying with C leads to the inhibition of xo-phase formation, as already shown for high Nb containing γ-TiAl based alloys, termed TNB alloys [22].

Ensuing re-heating with a rate of ≈2 K min-1 from 750 to 1200 °C and subsequent quenching (Fig. 2) leads to the formation of a microstructural condition, as displayed in Fig. 3c. The originally coarse-grained α2/γ-colonies with a very small thickness of the γ-lamellae were refined to a fine-grained α2/γ-phase arrangement composed of γ- and α2-phase, as likewise reported for a TNB alloy with a composition of Ti–45Al–7.5Nb [10]. The refinement of microstructure is the result of discontinuous coarsening or the so-called cellular reaction (CR), where a reaction front moves throughout the a2/c-colonies starting from the colony boundaries decomposing the coarse-grained and fine-lamellar colony structure to a refined microstructure (α2/γ)CR [23]. This microstructural instability, however, is more pronounced with increasing temperature due to enhanced thermal activation of diffusion processes. After re-heating to 1200 °C, p-type carbides are completely dissolved in the γ-matrix and the microstructure consists of ≈97 vol.% of refined (α2/γ)CR area, 2 vol.% βo-phase and a residual content of 1 vol.% of h-type carbides and Tiborides. The resulting microstructure is reflected in a decrease of macrohardness to 410 HV10 due to (i) the dissolution of p-type carbides, (ii) the alteration of the fine-spaced lamellar colonies and (iii) the coarsening of γ-phase within (α2/γ)CR, which is the softest phase in the TNM alloy system [21,24].

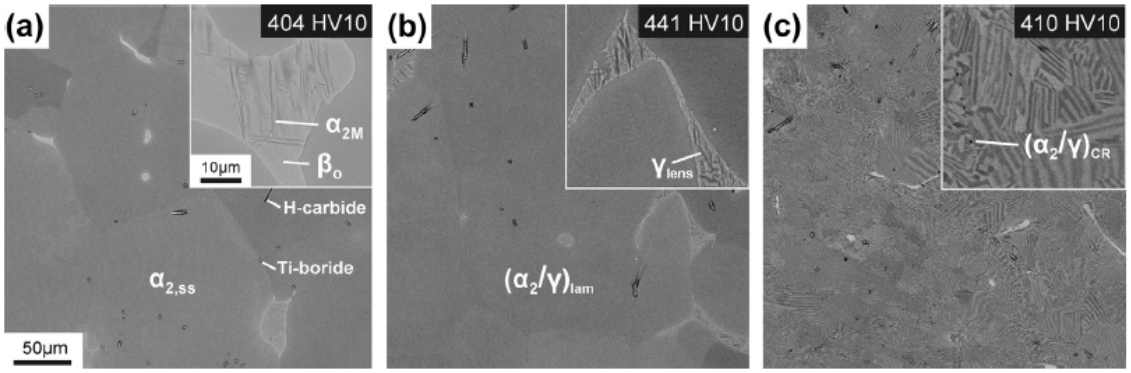

Fig. 3. SEM micrographs in BSE mode corresponding to the characteristic thermal conditions as given in the T–t diagram in Fig. 2. (a) The microstructure after the first heat-treatment step primarily consists of supersaturated a2-grains (α2,ss). Due to quenching from 1415 °C the βo-phase is interspersed with martensitic-type αo 2-laths (α2M). (b) Precipitation annealing at 750 °C for 4 h leads to the formation of α2/c-colonies and lens-shaped γ-grains within the βo-phase. (c) Re-heating with 2 K min-1 to 1200

°C subsequent to the isothermal segment yields to a refinement of the α_2/γ-grains by means of a cellular reaction (CR). In addition the macrohardness according to Vickers (HV10) is indicated.

3.2. HEXRD streaking

From the comparison of the 2-D diffraction patterns shown in Fig. 4a and b, corresponding to the supersaturated as well as isothermally annealed states, respectively, it is obvious that the precipitation of fine, geometrically well-defined microstructural features leads to the occurrence of diffraction streaks, i.e. anisotropic peak broadening (Fig. 4b). In a previous work, the occurrence of streaking, reported by Liss et al. [10] for a C-free TNB alloy with a composition of Ti–45Al–7.5Nb, was attributed mainly to the finite thickness of the lamellar crystallite composite consisting of α_2- and γ-laths. Especially in the early stages of precipitation, the features of the lamellar colonies remain very fine, leading to straight and narrow lines within the 2-D diffraction patterns. However, the change of the nanostructure during continuous heating, i.e. increasing thickness of c-lamellae with temperature as well as discontinuous coarsening of nanofeatures, causes the disappearance of diffraction streaks. Additionally, chemical gradients and phonon interactions were quoted as possible reasons for the appearance of diffraction streaks [10].

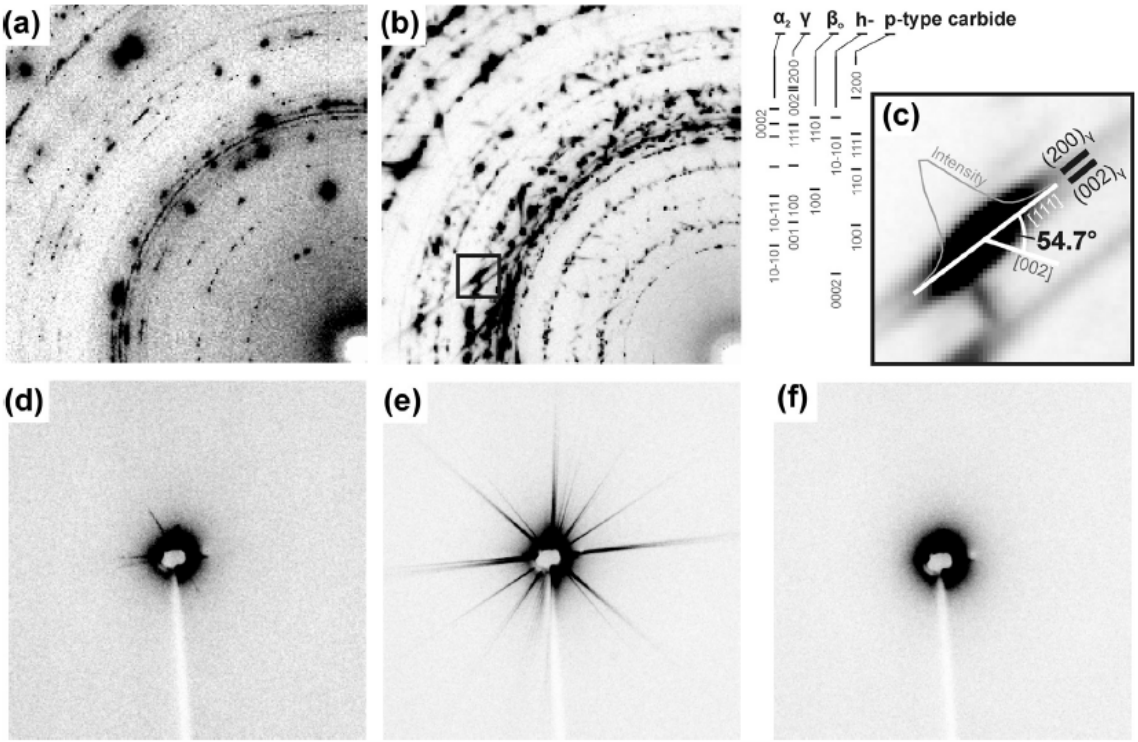

Fig. 4. HEXRD detector images (a) after the thermal treatment at 1415 °C for 1 h and quenching; (b) after a subsequent precipitation annealing at 750 °C for 4 h. The image section in (c) corresponds to a detail of the streaked $(002)_\gamma$ and $(200)_\gamma$ reflections as indicated as a framed area in (b). SAXS detector images (d–f), where (d) correlates to the supersaturated heat-treatment condition in (a) and (e) to the annealed state in (b). (f) Heat-treated condition after isothermal annealing, re-heating to 1200 °C and quenching.

An α_2/γ-colony in the [0_11]-zone axis is schematically shown in Fig. 1 in correspondence to the diffraction setup used. There, the Blackburn OR yields to a strictly defined geometrical arrangement where the $(0001)\alpha_2$ and $(111)\gamma$ lattice planes are parallel (note the definition of the coordinate system of the γ-phase in Fig. 1). Additionally, in the [0_11]-zone axis the $(111)\gamma$ planes are in the diffraction condition, whereas the further two equivalents from the $\{11\ 1\}\gamma$ family do not contribute to the diffraction signal. The four variants of $\{1\ 11\}\gamma$ span a tetrahedron, which can also be interpreted as a pair of two crossed $\{1\ 11\}\gamma$ planes, creating a characteristic angle of 70.1°, e.g. between $(111)\gamma$ and $[111]\gamma$. The crystallographic structure of the α_2/γ-phase compound leads to a 2-D diffraction pattern depicted in a simplified way in Fig. 1. The diffraction spots of the characteristic, phase-specific atomic planes are defined by means of the normal vector and the lattice spacing for a fixed sample-to-detector distance and monochromatic wavelength.

In the case of the schematic drawing in Fig. 1 the diffracting α_2/γ-colony from the polycrystalline composite is tilted through an angle φ around the [0_11]-zone axis, which is parallel to the normal vector of the detector plane. On the one hand, the $(111)_c$ plane leads to a nearly undistorted diffraction spot along the $[111]\gamma$ direction, as depicted within the detector plane. Therein, the distortion is mainly influenced by the projection and the alignment of the detector. Additionally, it is also possible that $(111)\gamma$ causes a diffraction spot mirrored around the beam stop, as indicated by the dotted line in the schematic HEXRD pattern in Fig. 1. However, only one of these mentioned (11 1)γ reflections can occur simultaneously.

On the other hand, the [-111]γ lattice planes yield to a diffraction spot oriented in the [_111]γ direction, which exhibits a very anisotropic shape and is elongated in the [111]γ direction. This means that [11 1]γ, or $[0001]\alpha_2$, is the direction where streaking occurs. This fact implies that only the horizontal component in the crystal-coordinate system of [_111]γ contributes to the streaking phenomenon and thus leads to a vertical distortion of the diffraction signal.

The difference in the diffraction signal from (111)γ and [_111]γ lattice planes has to be considered in more detail. (111)γ exhibits a strict superordinate structure within a single α_2/γ-colony, i.e. all (11 1)γ planes of neighboring γ-lamellae are parallel and contribute to interference when in diffraction condition, which results in a sharp and nearly isotropic diffraction spot. In contrast, the Blackburn OR in correlation to the crystal symmetries of the α_2- and γ-phase allow the formation of six different orientation variants of [_111]γ leading to a rotational symmetry around [111]γ between neighboring c-lamellae and/or appropriate domains within a γ-lamellae. Therefore, no strict superordinate structure exists for [_111]γ, which causes a significant peak broadening in the 2-D diffraction pattern in the [111]γ direction due to a lower number of coherently diffracting domains when compared to (111)γ. The presence of twinning, e.g. mechanical or annealing twins, can lead to the formation of additional mirrored reflections and streaks. However, without twinning, a maximum of two streaks can occur from a single α_2/γ-colony, i.e. from the “normal” [_111]γ as well as its 180^{o} domain variant when simultaneously present within a single α_2/γ-colony. In general, the interpretation of this phenomenon is more difficult in the case of a polycrystalline phase compound due to the existence of ambiguities depending on grain statistics. In the current case, the diffraction data prove that the geometrical conditions contribute as the dominating mechanism to streak formation. After precipitation annealing for 4 h at 750 ^{o}C, chemical gradients, e.g. arising from an inhomogeneous distribution of alloying elements resulting in a gradual course of the phase-specific lattice parameters, seem to be negligible because sharp interfaces with a low misfit between the α_2- and γ-phase as well as small diffusion pathways are present. For example, see the TEM bright-field image of the nanostructure shown in Fig. 5a. Furthermore, no indications of phonon interaction were found as significant contribution to streak formation.

In conclusion, diffraction streaking of an α_2/γ-colony requires (i) a layered and, therefore, anisotropic crystallite structure, (ii) a fine dimension of α_2- and γ-lamellae thickness within the α_2/γ-composite, (iii) the 60^{o}-stepwise rotational symmetry of [_111]γ lattice planes around the [111]γ axis as well as (iv) that [_111]γ lattice planes have to be in diffraction condition.

Depending on the Blackburn OR multiple phase-specific spots occur simultaneously in the streak direction, e.g. $[20\_22]\alpha_2$ reflection as depicted in Fig. 1 (compare with the experimental diffraction pattern in Fig. 4b). The peak overlap of {11 1}γ with $(0001)\alpha_2$ makes it necessary using a non-superimposed peak for the correlation of the peak width in the [111]γ direction with the thickness of γ-lamellae according to Eq. (1). Therefore, the peak broadening was determined from the (002)γ and (200)γ double reflection, as shown in Fig. 4c, which is an enlarged view of the framed area in Fig. 4b, by integrating over the Bragg angle yielding to a Gaussian peak shape. The Scherrer formula in Eq. (1) assumes that peak broadening solely is caused by small dimensions of the diffracting crystallites. The contribution of defects and micro-strain to the peak broadening is not considered here, since it can be neglected because of the thermal history. Annealing at 750 ^{o}C for 4 h leads to defect obliteration and relief of residual stresses of second and third order. The instrumental broadening was determined from powder diffraction measurements employing a LaB_6 standard by subtracting the FHWM of similarly located $(200)LaB_6$ at a coincident peak height when compared to the consolidated (002)γ and (200)γ double reflection. The evaluation of the anisotropically broadened peak in Fig. 4c by using Eq. (1) results in a characteristic dimension of 6.2 nm of the corresponding diffraction streak, which can be associated with the average thickness of the ultra-fine γ-laths. The FWHM in the [11 1]γ

direction corresponds directly to the average thickness of the diffracting γ-lath without further conversion because peak broadening is caused by the horizontal component of the {_111}γ, as indicated for the arrangement shown in Fig. 1.

Generally, a more pronounced increase in peak width is attributed to a smaller dimension of γ-lamellae. Therefore, primarily the smaller γ-lamellae can be accurately assigned to the corresponding crystal dimensions by applying HEXRD measurements on a polycrystalline material exhibiting a lamellar microstructure. Presuming that the growth of p-type carbides is controlled by the thickness of c-lamellae, the characteristic dimensions of p-type carbides can be determined to a length of 11.2 nm and a radius of 0.8 nm by applying the geometrical correlation $D = 2\mu R \times \cos(54.7^{o})$, where D corresponds to the average thickness of the γ-laths and μ is the size aspect ratio of the particles (μ = 7, see also Fig. 1). Thereby, the angle of ≈54.7° correlates to the tilting between [111]γ and [002]γ, which in turn is attributed to the angle spanned from the “thickness vector” of a γ-lath and the “length vector” of a p-type carbide, respectively (compare Fig. 4c). The corresponding nanofeatures of the heat-treatment state in Fig. 4b and c are depicted in Fig. 5. The representative TEM bright-field images are in agreement with the results gained from HEXRD measurements. While from HEXRD only a γ-lath thickness of 6.2 nm was obtained from a single diffraction streak, the TEM image in Fig. 5a reveals a size distribution of the γ-lamellae in the range of 5–30 nm. The TEM micrograph of the p-type carbide structure within a characteristic γ-lath of the α_2/γ-colony (Fig. 5b) confirms the shape model and the size aspect ratio of μ = 7. The needle-like p-type carbides are aligned along [001]γ, as mentioned in Fig. 1, and their size is restricted by the thickness of the appropriate γ-lath. Furthermore, during isothermal annealing no p-type carbide precipitation in the α_2-phase took place, as also recently reported for a TNM alloy with 1.5 at.% Mo and 0.5 at.% C [7].

3.3. Carbide precipitation and thermal stability

The SAXS detector images of the characteristic heat treatment states are depicted in Fig. 4d–f. All images show a pronounced small-angle scattering signal around the beam stop. The supersaturated condition prior to aging (Fig. 4d) exhibits a few small streaks, which are caused by the martensitic structure of the α'_2-phase formed during quenching within the b_o-phase. These streaks vanish during the initial stage of the isothermal precipitation annealing (aging) step at 750 °C. After a distinct incubation time, streaking occurs as exemplarily given in Fig. 4e for the heat-treatment condition after 4 h. The formed streaks are more pronounced than those mentioned for the martensitic structure in Fig. 4d and, therefore, assigned to smaller structural features within the formed hierarchical structure. The distinct incubation time for nucleation rules out the precipitation of ultra-fine c-lamellae contributing to the current SAXS signal because the c-phase precipitation from the supersaturated condition occurs immediately after thermal activation at T > 720 °C [25,26]. The occurring streaks appear as strong centrosymmetric lines originating in the directional alignment of p-type carbides within a γ-lath, as schematically shown in Fig. 1. The different streak lengths in the 2-D SAXS image are caused by a dissimilar mapping of the carbide structure within the polycrystalline microstructure as well as a carbide size distribution resulting from the size distribution of the γ-laths within the individual colonies (see Fig. 5). Further heating to 1200 °C after isothermal annealing leads to disappearance of streaking as depicted in Fig. 4f, which can be attributed to the dissolution of p-type carbides within the γ-matrix.

Selected azimuthally averaged scattering curves during isothermal annealing and subsequent heating to 1200 °C are shown in Fig. 6. The zero point on the time scale refers to the beginning of the isothermal segment. Additionally, the influence of the martensitic structure on the evolution of scattering curves was neglected in order to illustrate the effect of p-type carbide precipitation on the scattering curve profiles. There, the magnitude of the scattering vector q corresponds in an inverse relationship to the characteristic dimensions, i.e. radii, of the precipitated particles, whereas the macroscopic scattering cross-section $d\Sigma/d\Omega$ is directly proportional to the fraction and number of p-type carbide precipitations. After the disappearance of the martensitic contribution and a distinct incubation time of p-type carbide nucleation of several minutes, the scattering curves increase in $d\Sigma/d\Omega$ and shift to larger q up to an annealing time of 333 min, as shown in Fig. 6a, which is already in the re-heating segment of the heat treatment. Further annealing decreases $d\Sigma/d\Omega$ (Fig. 6b).

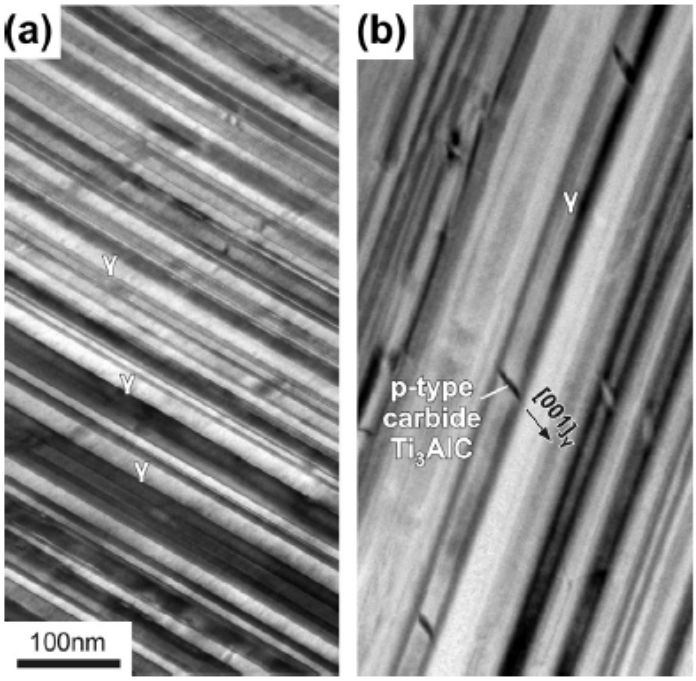

Fig. 5. (a) TEM bright-field image of an α_2/γ-colony in $[11\_20]_{\alpha_2}$- and <10_1>γ-zone axis. (b) TEM bright-field image of p-type carbides aligned within a characteristic c-lath according to the scheme shown in Fig. 1. The material under consideration was heat-treated at 750 °C for 4 h, leading to the microstructure shown in Fig. 3b.

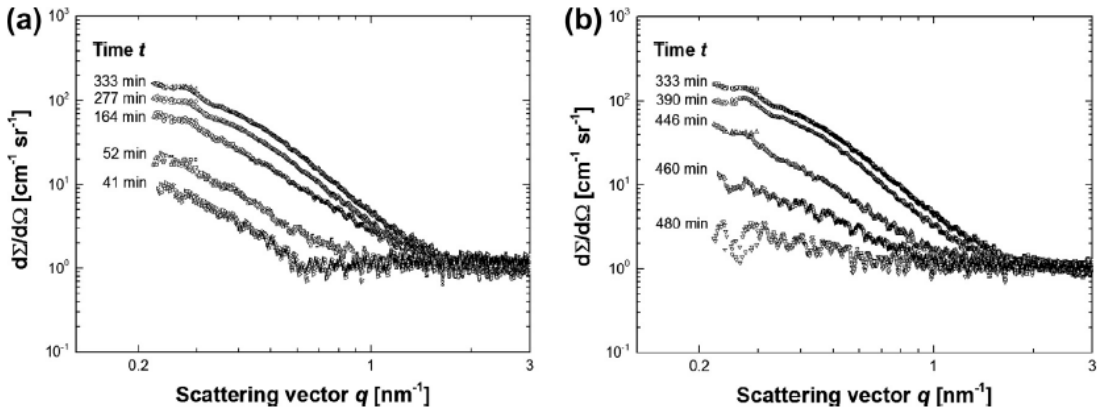

Fig. 6. (a) Scattering curves during the in situ SAXS experiment as a function of time with increasing and (b) decreasing evolution of the maximum of the macroscopic scattering cross-section $d\Sigma/d\Omega$. Note that the scattering curves were background-corrected to 1 cm^{-1} sr^{-1}.

Evaluation of the scattering curves (Fig. 6) allows describing carbide precipitation kinetics as well as their thermal stability, as summarized in Fig. 7. After the beginning of isothermal annealing at 750 °C, nucleation of p-type carbides needs _30 min to start. This incubation time is due to the need for prior c-phase formation and the slow diffusion rate of relevant elemental species. However, γ-laths are formed relatively fast from the supersaturated condition [25,26]. P-type carbide formation is determined by slower diffusional processes within the γ-phase according to the phase transformation pathway $\alpha_{2,ss} \rightarrow \alpha_2 + \gamma$ and $\gamma \rightarrow$ p-Ti_3AlC. The mechanism determining the rate of nuclei formation is seen in a local enrichment of Ti and other alloying elements, e.g. Nb and Mo, in order to transform the γ-TiAl stoichiometry to a nuclei with a composition of Ti_3AlC (containing small amounts of Nb and Mo). After 1 h, the precipitated carbide particles have reached a constant mean radius R_0 of ≈1.7 ± 0.3 nm, which is stable until the end of the isothermal annealing step (Fig. 7). Therein, R_0 corresponds to the modal value of the size distribution. After 3–4 h, a volume fraction f of 2.5 ± 0.5% p-type carbides was formed within the γ-phase corresponding to a precipitated particle number density n of ≈8.9 x 10^{16} cm^{-3}. Because of the absolute intensity calibration of the particle volume via Rietveld analysis as well as

uncertainties in the SLDD and the particle shape evolution during annealing, a relative inaccuracy of _20% for the refined precipitation volume has to be considered.While an error in the calibration and the calculated SLDD would shift the volume fraction curve as a whole, changes to the SLDD during heating would change the shape of the curve. During the isothermal heat treatment (segment 1), the measured length change DL decreases from 166 lm to 147 lm, reaching a nearly stable plateau. The zero point of the DL-scale is set at RT. The results are in good agreement with a SANS measurement performed on a Ti–48.5Al–0.4C alloy after precipitation annealing at 750 °C for 24 h, where a mean radius of 1.7 nm, a particle number density of 5.4 X 10^{16} cm^{-3} and a total particle volume fraction of 1.5% had been determined [9]. In the case of the investigated TNM–1C alloy the amount of p-type carbides is increased due to a higher C-content, although a decreased amount of Al and alloying with Nb and Mo contribute to a higher solubility for C [7,8,27].

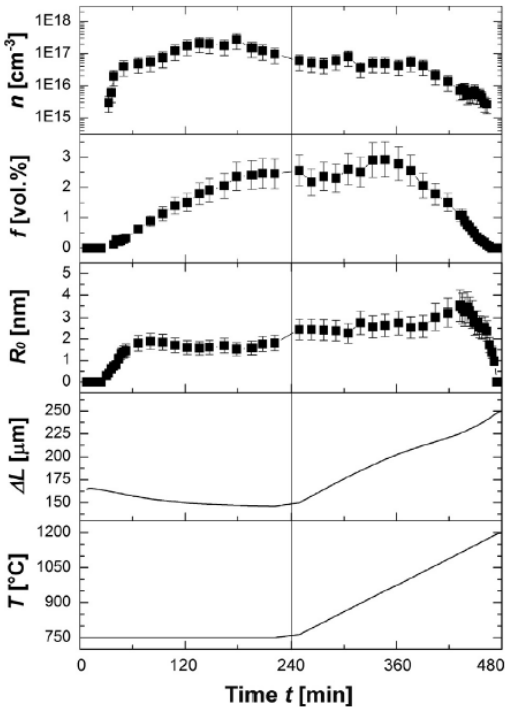

Fig. 7. Progress of temperature T and length change DL of the dilatometer sample during the precipitation heat-treatment step. Additionally, the mean radius R_0 of the needle-shaped p-type carbide precipitates, their volume fraction f in relation to the c-phase content and their number density n are indicated as evaluated from the in situ SAXS measurement.

The ensuing heating step with a rate of 2 K min^{-1} to 1200 °C (segment 2) was conducted to investigate the thermal stability of the extremely-fine precipitated p-type carbides. During heating, the volume fraction of p-type carbides increases to a maximum of 2.9% at 950 °C. At temperatures above 950 °C the carbides still coarsen until a maximum size of ≈3.5 nm is reached at 1130 °C. Between 1130 and 1185 °C the carbide precipitates dissolve within the matrix, which is primarily caused by increased C-solubility with higher temperature. The low heating rate of 2 K min^{-1} allows determining the dissolution temperature of the p-type carbides Ti_3AlC close to thermodynamic equilibrium condition to 1185 ± 5 °C. The carbide size distribution was evaluated from the scattering curves of the in situ SAXS experiment. Due to the low sample-to- detector distance and high photon energy of 100 keV, the smallest scattering vector was limited to 0.2 nm^{-1}. A pronounced background around the beam stop further reduced the useful q-range. However, a size aspect ratio of μ = 7, as verified by TEM investigations on the TNM–1C material (compare Fig. 5), provides satisfying results when data fitting is performed.

The size distribution of p-type carbides after isothermal annealing at 750 °C for 4 h is shown in Fig. 8. R and D are coupled by the geometrical relation D = 2μR x cos(54.7°), as mentioned in Section 3.2. The obtained monodisperse size distribution is caused by the simultaneous precipitation of γ-laths and thus p-type carbides have to develop from a completely supersaturated a_2-phase, i.e. no γ-lamellae formation took place during quenching. Therefore, no polydisperse size distribution could be developed from a pre-existent c-phase fraction. The data evaluation from the in situ SAXS measurement shows good agreement with the TEM results (Fig. 5b) with respect to the minimum and

maximum characteristic dimensions, i.e. the p-type carbides exhibit a sharp R-distribution with R_0 = 1.7 nm, corresponding to a carbide length of 23.8 nm and a mean c-lamellae thickness D_0 of 13.8 nm. The distribution of γ-lath thickness, i.e. in the range of 4–50 nm, agrees well with the TEM measurements of ≈5–30 nm (see Fig. 5a). However, the geometrical correlation between R and D is only valid as long as the growth of p-type carbides is controlled by the thickness of c-lamellae, i.e. at a maximum of 1130 °C where the size of carbides reduces due to thermodynamic reasons, i.e. increased solubility of the matrix for C. Furthermore, the data gained from the in situ SAXS measurement are in good agreement with the observed streaking from HEXRD, as mentioned in Section 3.2, where the peak broadening of the originally ultra-fine γ-lath was evaluated, i.e. 6.2 nm lath thickness, which correlates with a typical size of p-type carbides of 0.8 nm in radius and 11.2 nm in length.

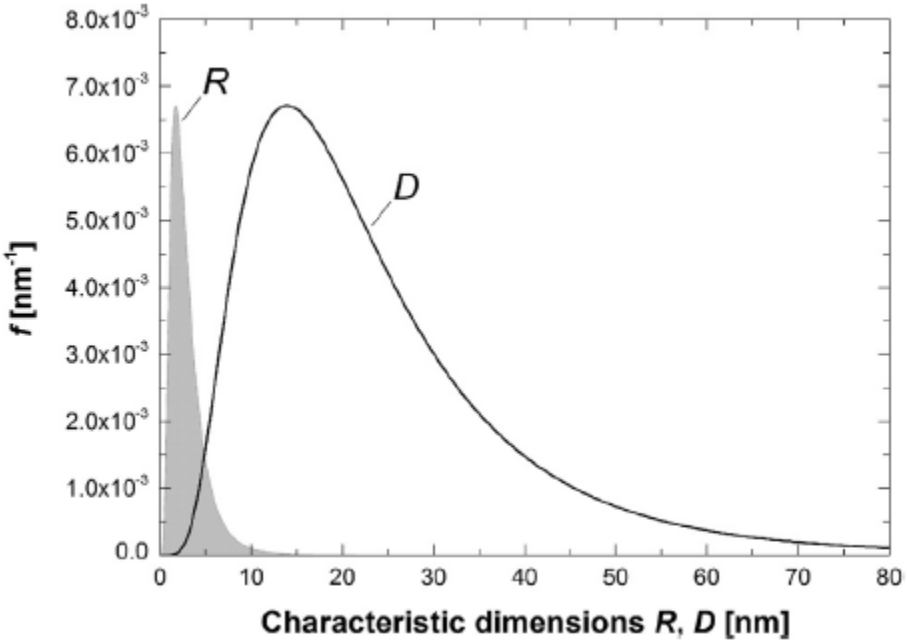

Fig. 8. Size distribution of p-type carbides Ti_3AlC after the aging step at 750 °C for 4 h as a function of radius R and corresponding c-lath thickness D, obtained from the geometrical correlation D = 2μR x cos(54.7°) by using a size aspect ratio of the p-type carbides of μ = 7 (see text).

4. Conclusions

The formation of ultra-fine needle-shaped p-type carbides Ti_3AlC aligned within the nanometer-scaled γ-laths of lamellar α_2/γ-colonies does not lead to a pronounced increase in hardness and yield strength when compared to a C-free TNM alloy. Nevertheless, p-type carbide precipitation effectively reduces the dislocation mobility during dislocation creep, as reported for a C-containing TNM alloy with 1.5 at.% Mo and 0.5 at.% C [7].

The conducted in situ small-angle X-ray scattering experiment with synchrotron radiation starting from a supersaturated TNM–1C alloy allows us to determine the precipitation behavior during isothermal annealing at 750 °C as well as the thermal stability of p-type carbides during further heating to 1200 °C with a rate of 2 K min^{-1}. It was found that p-type carbide formation takes place after an incubation time of 30 min within the γ-laths previously formed from supersaturated α_2-grains. Thus, the phase-transformation sequence takes the form $\alpha_{2,ss} \rightarrow \alpha_2 + \gamma$ and $\gamma \rightarrow$ p-Ti_3AlC. After aging for 4 h at 750 °C, the carbide precipitates exhibit a mean radius of 1.7 nm – obeying a monodisperse size distribution – which correlates with a carbide length of 23.8 nm and a mean γ-lamellae thickness of 13.8 nm. Thereby, the thickness D of γ-laths and the radius R of p-type carbides are correlated by the geometrical relation D = 2μR x cos(54.7°) according to the OR $(001)_\gamma \parallel (001)_p$ and $(010)_\gamma \parallel (010)_p$. The needle-shaped p-type carbides exhibit a typical size aspect ratio of l = 7 as verified by TEM. The geometrical correlation is valid as long as the size of p-type carbides is controlled by the small dimension of c-lamellae. As a consequence, the distribution of c-lamellae thickness can be easily determined from the evaluation of the radius distribution of p-type carbides from SAXS without expensive and time-consuming TEM effort.

Complementarily, the data from SAXS are in good agreement with the evaluation of diffraction streaks from the 2-D HEXRD patterns using the Scherrer equation. The occurrence of diffraction streaks, i.e. anisotropic peak broadening, was found to originate from the finite thickness of γ-laths and the geometrical relation between the monochromatic X-ray beam and the structure of an α_2/γ-colony within the polycrystalline TNM–1C material. Diffraction streaking implies that the 70.1^{o} tilted $(\_111)\gamma$ lattice planes are in diffraction condition, and do not exhibit a strong superordinate structure when compared to $(111)\gamma$ lattice planes which are by definition parallel to $(0001)\alpha_2$.

During the subsequent heating step a maximum amount of ≈2.9 vol.% p-type carbides is precipitated within the γ-phase at 950 ^{o}C, exhibiting amean radius of 2.6 nm. Above 950 C the volume content of carbides decreases in accordance with the thermodynamic equilibrium, whereas particle coarsening yields to a maximum size of p-type carbides showing a mean radius of 3.5 nm at 1130 ^{o}C. At higher temperatures, the carbide precipitates dissolve within the matrix until their dissolution temperature of 1185 ^{o}C is reached.

Acknowledgments

The authors gratefully thank Rene´ Kirchhof, Torben Fischer and Lars Lottermoser for their assistance at the beamline, Gerhard Hawranek for professional SEM operation and Gabriele Moser for advanced TEM sample preparation. This work received funding from the German BMBF project O3X3530A and the European Community's 7th Framework Programme (FP7/2007e2013) under grant agreement no. 226716.

References

[1] Kim YW, Morris D, Yang R, Leyens C. Structural aluminides for elevated temperature applications. Warrendale, PA: TMS; 2008.
[2] Appel F, Paul JDH, Oehring M. Gamma titanium aluminide alloys: science and technology. Weinheim: Wiley-VCH; 2011.
[3] Clemens H, Mayer S. Adv Eng Mater 2013;15:191.
[4] Kawabata T, Tadano M, Izumi O. ISIJ Int 1991;31:1161.
[5] Tian WH, Nemoto M. Intermetallics 1997;5:237.
[6] Christoph U, Appel F, Wagner R. Mater Sci Eng A 1997;239–240:39.
[7] Schwaighofer E, Rashkova B, Clemens H, Stark A, Mayer S. Intermetallics 2014;46:173.
[8] Scheu C, Stergar E, Schober M, Cha L, Clemens H, Bartels A, et al. Acta Mater 2009;57:1504.
[9] Staron P, Christoph U, Appel F, Clemens H. Appl Phys Mater Sci Process 2002:74.
[10] Liss KD, Stark A, Bartels A, Clemens H, Buslaps T, Phelan D, et al. Adv Eng Mater 2008;10:389.
[11] Scherrer P. Nachrichten Von Ges Wiss Zu Go¨ tt Math-Phys Kl 1918;1918:98.
[12] Langford JI, Wilson AJC. J Appl Crystallogr 1978;11:102.
[13] Monshi A. World J Nano Sci Eng 2012;02:154.
[14] Glatter O, Kratky O. Small angle X-ray scattering. London: Academic Press; 1982.
[15] Hammersley AP, Svensson SO, Hanfland M, Fitch AN, Ha¨usermann D. High Press Res 1996;14:235.
[16] Schmoelzer T, Liss K-D, Staron P, Mayer S, Clemens H. Adv Eng Mater 2011;13:685.
[17] Schwaighofer E, Clemens H, Mayer S, Lindemann J, Klose J, Smarsly W, et al. Intermetallics 2014;44:128.
[18] Djanarthany S, Servant C, Penelle R. J Mater Res 1991;6:969. [19] Blackburn MJ. Scientific and technological applications of titanium. Oxford: Pergamon Press; 1970.
[20] Kurdjumow G, Sachs G. Z Phys 1930;64:325.
[21] Schloffer M, Rashkova B, Schoeberl T, Schwaighofer E, Zhang Z, Clemens H, et al. Acta Mater 2014;64:241.
[22] Stark A, Bartels A, Clemens H, Schimansky F-P. Adv Eng Mater 2008;10:929.
[23] Denquin A, Naka S. Acta Mater 1996;44:353.
[24] Schloffer M, Iqbal F, Gabrisch H, Schwaighofer E, Schimansky FP, Mayer S, et al. Intermetallics 2012;22:231.
[25] Cha L, Schmoelzer T, Zhang Z, Mayer S, Clemens H, Staron P, et al. Adv Eng Mater 2012;14:299.
[26] San Juan J, Simas P, Schmoelzer T, Clemens H, Mayer S, No´ ML. Acta Mater 2014;65:338.
[27] Menand A, Huguet A, Ne´rac-Partaix A. Acta Mater 1996;44:4729.